

Fractional quantum Hall effect in the interacting Hofstadter model via tensor networks

M. Gerster,¹ M. Rizzi,² P. Silvi,^{1,3} M. Dalmonte,⁴ and S. Montangero^{5,1}

¹*Institute for Complex Quantum Systems & Center for Integrated Quantum Science and Technology (IQST), Ulm University, Albert-Einstein-Allee 11, D-89069 Ulm, Germany*

²*Institut für Physik, Johannes Gutenberg-Universität Mainz, Staudingerweg 7, D-55099 Mainz, Germany*

³*Institute for Theoretical Physics, University of Innsbruck, A-6020 Innsbruck, Austria*

⁴*Abdus Salam International Center for Theoretical Physics, Strada Costiera 11, Trieste, Italy*

⁵*Theoretische Physik, Universität des Saarlandes, D-66123 Saarbrücken, Germany*

(Dated: 19th May 2017)

We show via tensor network methods that the Harper-Hofstadter Hamiltonian for hard-core bosons on a square geometry supports a topological phase realizing the $\nu = 1/2$ fractional quantum Hall effect on the lattice. We address the robustness of the ground state degeneracy and of the energy gap, measure the many-body Chern number, and characterize the system using Green functions, showing that they decay algebraically at the edges of open geometries, indicating the presence of gapless edge modes. Moreover, we estimate the topological entanglement entropy, which is compatible with the expected value $\gamma = 1/2$. Finally, we describe the phase transition from a FQH state to density wave states as a function of a staggered chemical potential. Our results provide extensive evidence that FQH states are within reach of state-of-the-art cold atom experiments.

PACS numbers: 37.10.Jk, 05.10.Cc, 71.10.Pm, 73.43.Nq

Introduction – The Harper-Hofstadter model [1] plays an archetypical role in the current understanding of topological quantum matter on a lattice. It encompasses the basic coupling between particles and a background magnetic field, and supports topological bands with finite Chern number for a broad range of fluxes and tunneling rates [2]. Those remarkable properties have motivated proposals [3] and recent experiments in both solid-state [4] and cold atom systems [5–9], which have extensively investigated its non-interacting limit, including the observation of its fractal spectrum [4] and the measurement of a finite Chern number [8] in some of its bands. More recently, experiments using bosonic atoms in optical lattices have shown impressive capabilities to approach the *strongly interacting* regime [7], with the ultimate goal of stabilizing lattice analogues of fractional quantum Hall (FQH) states [2, 10]. However, despite promising small system results based on exact diagonalization [11–14], in the large flux regime available to experiments – when the magnetic length is of order of the lattice spacing – theoretical evidence of such states at large scales has been lacking, especially regarding smoking guns of topological order – gapless edge modes, entanglement properties, and many-body Chern numbers.

In this work, we study the strongly-interacting bosonic Hofstadter model, and show that it supports a FQH ground state (GS) akin to the $\nu = 1/2$ Laughlin state in the continuum [10, 15, 16]. Our analysis is based on a combination of diagnostics, including GS degeneracies on different topologies, the measurement of the many-body Chern number, Green functions’ decay at the edge and in the bulk, and a direct measurement of the topological entanglement entropy. The corresponding results serve as a quantitative guideline to address the stability of such phases against temperature: crucially, we show how the

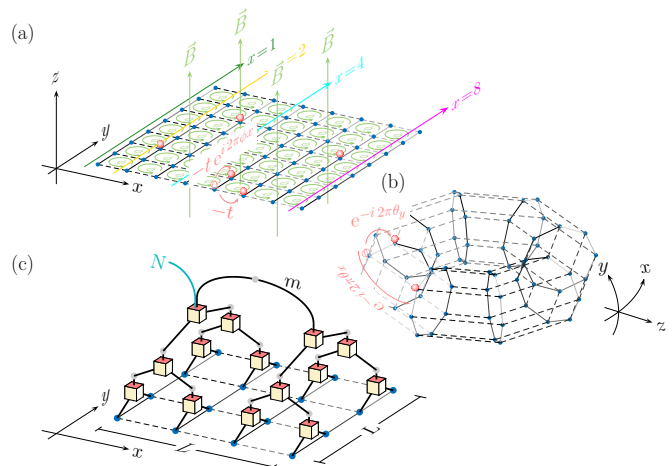


Figure 1. Sketch of the system for open (a) and periodic (b) boundary conditions (PBC). For PBC, phase twists θ_x and θ_y are introduced, allowing the definition of topological invariants. (c) Tensor network ansatz with bond dimension m , restricted to the subspace with N bosons in the system.

spectral gap of the bulk excitations is of the order of 10% of the tunneling rates, showing how FQH states are within reach for temperatures available to current experiments.

The enabling tool of our analysis are numerical simulations based on the tree-tensor network (TTN) ansatz [17, 18]. This class of tailored variational wave functions, whose concrete example used here is illustrated in Fig. 1c, extends the matrix-product state ansatz – the tensor network class at the heart of the density-matrix-renormalization group (DMRG) [19, 20]. To obtain the presented results on square lattices with sizes of up to 32×32 sites, we exploit the reduced scaling of compu-

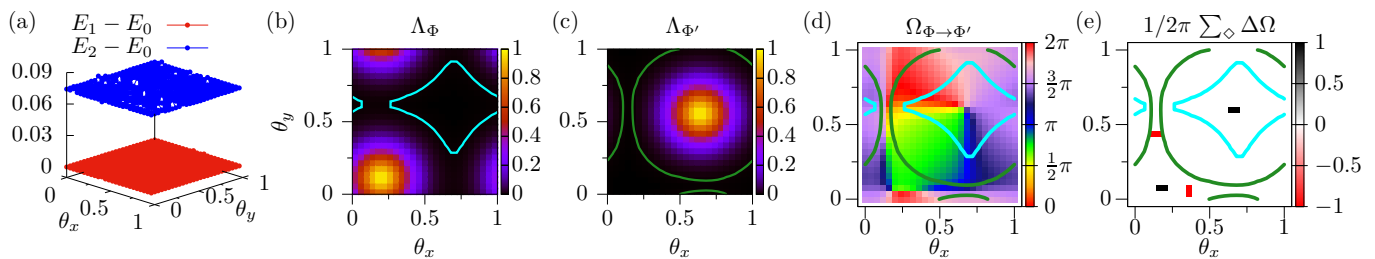


Figure 2. Low-lying spectrum (a) and many-body Chern number (MBCN) (b-e) for a system with $L = 16$, $N = 8$, $\phi = 1/16$ ($\nu = 1/2$). (a) Finite size spectrum as a function of the twist angles of the boundary conditions. The twofold degenerate GS manifold is separated from the first excited state by a gap $\Delta \simeq 0.08$. (b-c) Regions where Λ_Φ and $\Lambda_{\Phi'}$, respectively, vanish. The reference multiplet Φ , Φ' is composed of the two orthogonal GSs at $(\theta_x, \theta_y) = (0.2, 0.12)$, $(0.64, 0.56)$. (d) Color plot of the argument field $\Omega_{\Phi \rightarrow \Phi'}$, whose count of branch vortices gives the MBCN. (e) Location (and sign) of the branch points, obtained by summing up the angle differences $\Delta\Omega$ along the nearest neighbours of each grid point, resulting in a MBCN of one.

tational costs of the loopless geometry of TTNs, a characteristic not shared by other network structures such as PEPS and MERA [21].

Model Hamiltonian and methods – We study spinless bosonic particles hopping on a $L \times L$ square lattice under the influence of an external magnetic field, as illustrated in Fig. 1a-b. In the Landau gauge, the system is described by the following Hamiltonian [11]

$$H = U \sum_{x,y} n_{x,y} (n_{x,y} - 1) - t \sum_{x,y} \left\{ a_{x+1,y}^\dagger a_{x,y} e^{-i2\pi\delta_x L \theta_x} + a_{x,y+1}^\dagger a_{x,y} e^{i2\pi(\phi x - \delta_y L \theta_y)} + \text{h.c.} \right\} \quad (1)$$

of bosonic particles, $[a_{x,y}, a_{x',y'}^\dagger] = \delta_{x,x'} \delta_{y,y'}$, $n = a^\dagger a$. Here, ϕ is the magnetic flux through each plaquette (resulting in a magnetic filling factor $\nu = N/(\phi L^2)$, with N the number of bosons in the system) and θ_x, θ_y implement the twists in the boundary condition [12]. In the dilute limit (small densities and small fluxes) the lattice physics approaches the one of the continuum [22]. However, in the large flux limit, available in cold gases experiments, the phase diagram is not set. On small systems, it has been shown by exact diagonalization (ED) that the GS of the model described by Eq. (1) at filling factor $\nu = 1/q$ (where q is an even integer) is compatible with a lattice analogue of the (bosonic) Laughlin wave function [12–14, 23], exhibiting topological GS degeneracy and a non-zero Chern number [24]. However, the overlap with the exact Laughlin wave functions rapidly degrades with system size already for small systems of 6 particles. From a complementary viewpoint, the ladder version of the Hofstadter model has also been shown to share similarities with FQH states [25–27]. Very recently, iDMRG results on cylinders have shown strong signatures of integer quantum Hall states, and have reported fractional current quantization in regimes different from the one we consider here [28]. Throughout, we focus on the strongly interacting case $U \rightarrow \infty$ (hard-core bosons) with flux values $\phi = 1/8$ and $1/16$, which correspond to flux choices that are experimentally available. Finally, we set

$t = 1$ to fix the energy scale.

We employ a TTN ansatz [29] for the GS and the two lowest excited states to verify the properties discussed above. The accuracy of the TTN ansatz is controlled by the bond dimension m , and we exploit particle number conservation by restricting the ansatz to the N particle sector [30]. While it is known that a 2D-TTN is not compatible with the area law for the entanglement entropy [17, 30], it possesses a number of beneficial features which make it a promising tool for the study of intermediate system sizes: (a) The existence of a numerically stable search algorithm for eigenstates [18, 31]; (b) a low-order polynomial scaling $\mathcal{O}(m^4 L^2)$ of the computational cost; (c) easy interchange of various boundary conditions (open, periodic, twisted); (d) access to the entanglement entropy for bipartition shapes that enable the determination of the topological entanglement entropy (TEE) [32]. In what follows, we will exploit these properties to gather a number of numerical evidences for a FQH GS of the model Eq. (1) in the case of $\nu = 1/2$ filling.

Low-energy spectra – As first evidence we verify the GS degeneracy, intimately connected to the topological order of the system [10, 33]. On a torus geometry the GS degeneracy at $\nu = 1/2$ filling is expected to be twofold (independent of the twist angles θ_x, θ_y), while the first excited state is to be separated by a bulk gap. We determined the three lowest-energy eigenstates, reported in Fig. 2a: We clearly observe a finite energy gap $E_2 - E_0 \approx 0.1t$ which is typically more than two orders of magnitude larger than the energy difference $E_1 - E_0$ between the two states manifold (multiplet) in the GS for the system sizes considered here. Conversely, we verified that for open boundary conditions (OBC) the quasi-degeneracy is removed and we observe that $E_2 - E_1 \approx E_1 - E_0$.

Many-body Chern number – As second evidence we determine the many-body Chern number (MBCN) [24], which is a direct signature of topological order. For the numerical calculation of the MBCN we follow the prescription put forward by Hatsugai [34], which requires

the knowledge of the GS manifold on a 2D grid of twist angles $(\theta_x, \theta_y) \in [0, 1] \times [0, 1]$ (note that this grid also has a torus geometry). From a practical point of view, this method relies on the calculation of overlaps, a task which can be easily accomplished with TN states: More specifically, we need to choose two reference multiplets Φ, Φ' which have to be non-parallel but otherwise can be arbitrary. (Commonly, one picks two GS multiplets at twist angles far from each other [35].) This corresponds to two different gauge references, which can be used to define two scalar fields: $\Lambda_{\Phi^{(\prime)}} = \det\langle \Phi_j^{(\prime)} | P(\theta_x, \theta_y) | \Phi_k^{(\prime)} \rangle$, where the determinant runs over the indexes $j, k \in \{0, 1\}$ of the GS multiplet and $P(\theta_x, \theta_y) = |\Psi_0(\theta_x, \theta_y)\rangle\langle\Psi_0(\theta_x, \theta_y)| + |\Psi_1(\theta_x, \theta_y)\rangle\langle\Psi_1(\theta_x, \theta_y)|$ is the projector on the GS manifold at (θ_x, θ_y) . If the gauge has been fixed appropriately, Λ_{Φ} is well-defined (i.e. non-vanishing) where $\Lambda_{\Phi'}$ is not and vice versa, thus forming two complementary regions on the boundary condition torus (an example is shown in Fig. 2a-b). Finally, the MBCN is given by the number of branch vortices in the argument field $\Omega_{\Phi \rightarrow \Phi'} = \arg(\det\langle \Phi_j' | P(\theta_x, \theta_y) | \Phi_k \rangle)$, to be counted (with sign) in any of these two regions [34, 35]. We performed this procedure using TTN states; the result is shown in Fig. 2b-d. We obtain a MBCN of 1, clearly demonstrating the topological order in the GS of the model. Combined with the two-fold degeneracy discussed above, this shows that the system has a Chern number per state $C = 1/2$, as expected for the $\nu = 1/2$ Laughlin state.

Correlation functions and edge modes – Indirect evidence of a fractional quantum Hall state can also be gathered by monitoring the behavior of the Green function in the system $\mathcal{G}(x, x'; y, y') = \langle a_{x,y}^\dagger a_{x',y'} \rangle$. The Green function in periodic systems contains information about bulk excitations: in our case, it is expected to decay exponentially as a function of distance. In contrast, for open boundaries the Green function is expected to reveal the existence of gapless edge modes. Indeed, in the case of $\nu = 1/2$, the phase field operator of the corresponding chiral Luttinger liquid edge mode is expected to have considerable overlap with the creation and annihilation operators on the lattice. In Fig. 3a, we plot the normalized $\mathcal{G}(x, x; 1, y)$ as a function of y both for PBC and OBC. In the case of PBC, the results clearly show that \mathcal{G} decays exponentially as a function of distance, with a correlation length of approximately 2 sites - and thus, considerably smaller than our system sizes. Since for OBC translational invariance is broken, we consider different values of x (marked by different colors as also illustrated in Fig. 1a). Here, two distinct regimes are visible: long the edge (here for $x \lesssim 4$) the correlation decays as a power law, indicating a gapless mode localized close to the boundary. In sharp contrast, far from the edges ($x \simeq L/2$) the decay becomes exponential, consistent with the PBC results. Our results on the correlation functions thus strongly confirm a finite bulk gap, coexisting with gapless edge modes.

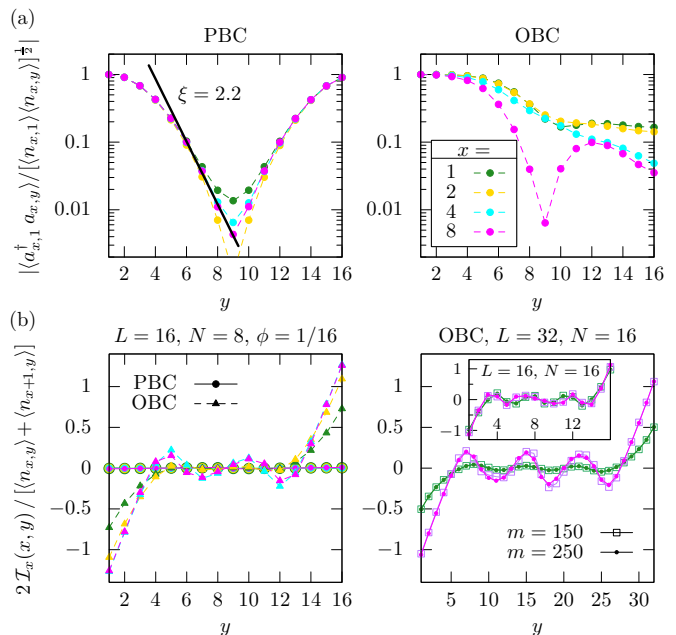


Figure 3. (a) Green functions along the y -direction for PBC (left) and OBC (right), for $L = 16, N = 8, \phi = 1/16$. In the PBC case the decay is exponential, irrespective of the choice of x . In contrast, for OBC, the decay at the edges ($x \approx 1$ or $y \approx L$) is much slower, signalling the presence of edge modes with algebraic correlations. (b) Current in the x -direction. Left plot: comparison between PBC (no current) and OBC (currents at the edges). Right plot: current for $L = 32, \phi = 1/32$ and for $\phi = 1/8, L = 16$ (inset) and $m = 150, 250$. All panels use the same color code for x , also illustrated in Fig. 1a.

An alternative route to detect chiral edge modes, likely more accessible in experiments, is given by the particle current density. Specifically, we consider here the current in the x -direction $\mathcal{I}_x(x, y) = i \langle a_{x+1,y}^\dagger a_{x,y} - a_{x+1,y} a_{x,y}^\dagger \rangle$, again both for PBC and OBC. In Fig. 3b we show the normalized $\mathcal{I}_x(x, y)$ as a function of y and for different values of x (again with the same color code). The results are in strong agreement with the ones obtained from the Green function analysis: For PBC, where there is only bulk, the current vanishes throughout the system, while for OBC we observe strongly enhanced currents along the edges, i.e. at $y \approx 1$ or $y \approx L$.

Topological entanglement entropy – An unambiguous indicator for topological order is the topological entanglement entropy (TEE) γ , as introduced in [32]. A finite value of γ signals the presence of anyonic excitations above the GS manifold - remarkably, without having to directly access excited states. In particular, γ is directly related to the quantum dimensions of the excitations. Extracting the TEE in numerical simulations is however challenging. System sizes available to exact diagonalization are typically too small to measure γ in a meaningful fashion. DMRG simulations can reach considerable

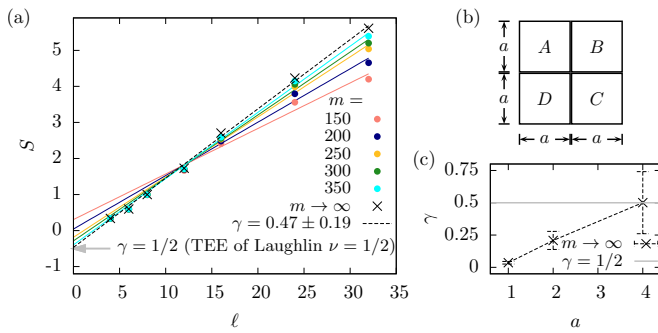


Figure 4. (a) TEE γ obtained from an extrapolation in m : Lines are linear fits through data points with $\ell > 10$, for $L = 16$, $N = 16$, $\phi = 1/8$. The resulting γ is compatible with $1/2$. (b) Arrangement of square partitions for the extraction of γ [32] and resulting TEE (c) as a function of the block size a . For large enough a , the data is compatible with $\gamma = 1/2$.

system sizes: in that context, one tries to extract the TEE γ as a correction to the perimeter-law scaling of the entanglement entropy: $S(\ell) = c\ell - \gamma$, where $S(\ell)$ is the von Neumann entropy $S = -\text{tr}[\rho \log_2 \rho]$ for a spatial partition of perimeter ℓ . In Fig. 4a, we show our results for $S(\ell)$ for PBC with $L = 16$. In order to avoid strong finite size effects, we excluded from our fits the data with $\ell < 10$. After extrapolation to $m \rightarrow \infty$, we get $\gamma = 0.49 \pm 0.19$, which is close to the value obtained with our maximum bond dimension. Despite the large error bar, mostly due to the fact that we have only access to few points in ℓ , our result show that the system has $\gamma > 0$, and the result is compatible with the expected TEE for a Laughlin state with $\nu = 1/q$, $\gamma = \log_2 \sqrt{q}$. While this procedure has been well tested in several models [36, 37], it is desirable to apply a method for obtaining the TEE which follows directly the original prescription: Such technique operates on regions with different shapes in order to exclude spurious effects. Within our TN ansatz this is possible considering the geometry in Fig. 4b, where it can be shown that the combination $S_A + S_B + S_C + S_D - S_{AB} - S_{BC} - S_{CD} - S_{DA} + S_{ABCD}$ equals $-\gamma$. The basic building block of this procedure are square partitions of size $a \times a$. The results of the corresponding simulations, extrapolated in $m \rightarrow \infty$, are shown in Fig. 4c: for $a = 4$ the results indicate a finite TEE of $\gamma \simeq 0.5$, again with rather large error bars (owing to the uncertainty in the m extrapolation), but otherwise in good agreement with the expected behavior for $\nu = 1/2$ FQH states. We note that for $a = 1, 2$ the results are far from this prediction, as expected, since for those values the partition size is smaller than the correlation length ξ as computed from the Green function decay.

Phase transition from FQH to trivial insulator – Finally, we investigate the robustness of the FQH state upon introducing a superlattice potential into the model from Eq. (1), which, in turn, can be engineered in cold

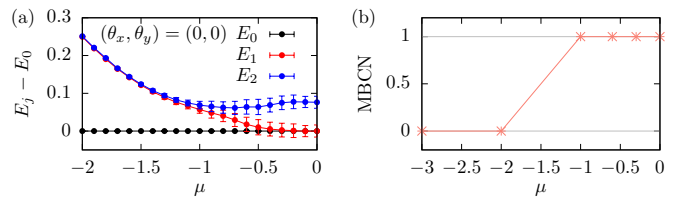


Figure 5. Transition from FQH (MBCN = 1) to topologically trivial phase (MBCN = 0) as a function of μ . System parameters are $L = 16$, $N = 8$, $\phi = 1/16$. (a) Three lowest eigenenergies of \tilde{H} as a function of μ , at $\theta_x = \theta_y = 0$. (b) MBCN as a function of μ , displaying a transition at $\mu_c \approx -1$.

atoms experiments [38]. We consider the Hamiltonian $\tilde{H} = H + \mu \sum_{(x,y) \in \text{sup.latt.}} n_{x,y}$, where $\mu \leq 0$ denotes the depth of the superlattice potential. Here, we focus on the case where the number of sites of the superlattice is equal to the number of bosons N in the system. For sufficiently large $|\mu|$, the GS of \tilde{H} is a product state with the particles pinned at the superlattice minima which is, by construction, topologically trivial. The transition between the two qualitatively different GSs occurs at some critical potential depth $\mu_c < 0$. In order to detect this transition we use the energy spectra on the boundary condition torus, and the MBCN, as shown in Fig. 5 and in [31]. With increasing depth of the potential, we observe how the GS quasi-degeneracy is removed. As long as the GS multiplet is still quasi-degenerate, i.e. separated from the first excited state ($E_2 - E_1 \gtrsim E_1 - E_0$) on the whole torus of twist angles, we measure a MBCN of one. At the critical point $\mu_c \approx -1.0$ this condition is no longer met and the MBCN vanishes, signaling a disappearance of the topological order.

Conclusions and outlook – We have presented extensive numerical evidence supporting the existence of a fractional quantum Hall phase in the Harper-Hofstadter Hamiltonian for hard-core bosons on a square lattice. Our analysis considered a wide range of independent diagnostics, including spectral properties, the many-body Chern number, correlation functions, currents, and entanglement entropies, and shows how TTN algorithms provide a flexible tool to address the interplay of gauge fields and interactions in two-dimensional systems. The results indicate that the correlation length is typically of the order of a few lattice sites, with corresponding gaps of order $0.1t$: these signatures point toward the fact that lattice fractional quantum Hall states can be realized in present cold atom experiments, given current temperature and size already available in experiments, and for which adiabatic state preparation protocols have very recently been shown to be applicable [28].

Acknowledgements – We thank M. Burrello and A. Sterdyniak for a careful reading of the manuscript, J. Budich and H.-H. Tu for discussions, and F. Tschirsich for contributing numerical libraries. Numerical calculations

have been performed with the computational resources provided by the bwUniCluster project [39], CINECA via the TEDDI project, and the MOGON cluster at the JGU Mainz. We acknowledge financial support from EU project RYSQ and UQUAM, the German Research Foundation (DFG) through the SFB/TRR21, OSCAR and TWITTER, and the Baden-Württemberg Stiftung via Eliteprogramm for postdocs. S.M. gratefully acknowledges the support of the DFG via a Heisenberg fellowship.

-
- [1] D. R. Hofstadter, *Phys. Rev. B* **14**, 2239 (1976).
- [2] B. A. Bernevig and T. L. Hughes, *Topological insulators and topological superconductors* (Princeton University Press, 2013).
- [3] J. Dalibard, F. Gerbier, G. Juzeliūnas, and P. Öhberg, *Rev. Mod. Phys.* **83**, 1523 (2011); D. Jaksch and P. Zoller, *New J. Phys.* **5**, 56 (2003); N. Goldman, G. Juzeliūnas, P. Öhberg, and I. B. Spielman, *Rep. Prog. Phys.* **77**, 126401 (2014).
- [4] C. R. Dean, L. Wang, P. Maher, C. Forsythe, F. Ghahari, Y. Gao, J. Katoch, M. Ishigami, P. Moon, M. Koshino, T. Taniguchi, K. Watanabe, K. L. Shepard, J. Hone, and P. Kim, *Nature* **497**, 598 (2013).
- [5] M. Aidelsburger, M. Atala, M. Lohse, J. T. Barreiro, B. Paredes, and I. Bloch, *Phys. Rev. Lett.* **111**, 185301 (2013).
- [6] H. Miyake, G. A. Siviloglou, C. J. Kennedy, W. C. Burton, and W. Ketterle, *Phys. Rev. Lett.* **111**, 185302 (2013).
- [7] C. J. Kennedy, W. C. Burton, W. C. Chung, and W. Ketterle, *Nat. Phys.* **11**, 859 (2015).
- [8] M. Aidelsburger, M. Lohse, C. Schweizer, M. Atala, J. T. Barreiro, S. Nascimbene, N. Cooper, I. Bloch, and N. Goldman, *Nat. Phys.* **11**, 162 (2015).
- [9] M. Mancini, G. Pagano, G. Cappellini, L. Livi, M. Rider, J. Catani, C. Sias, P. Zoller, M. Inguscio, M. Dalmonte, and L. Fallani, *Science* **349**, 1510 (2015); B. Stuhl, H.-I. Lu, L. Ayccock, D. Genkina, and I. Spielman, *Science* **349**, 1514 (2015).
- [10] E. Fradkin, *Field theories of condensed matter physics* (Cambridge University Press, 2013).
- [11] A. S. Sørensen, E. Demler, and M. D. Lukin, *Phys. Rev. Lett.* **94**, 086803 (2005).
- [12] M. Hafezi, A. S. Sørensen, E. Demler, and M. D. Lukin, *Phys. Rev. A* **76**, 023613 (2007).
- [13] G. Möller and N. R. Cooper, *Phys. Rev. Lett.* **103**, 105303 (2009).
- [14] A. Sterdyniak, N. Regnault, and G. Möller, *Phys. Rev. B* **86**, 165314 (2012).
- [15] V. Kalmeyer and R. Laughlin, *Phys. Rev. Lett.* **59**, 2095 (1987).
- [16] N. Regnault and B. A. Bernevig, *Phys. Rev. X* **1**, 021014 (2011).
- [17] L. Tagliacozzo, G. Evenbly, and G. Vidal, *Phys. Rev. B* **80**, 235127 (2009).
- [18] V. Murg, F. Verstraete, Ö. Legeza, and R. M. Noack, *Phys. Rev. B* **82**, 205105 (2010); N. Nakatani and G. K.-L. Chan, *J. Chem. Phys.* **138**, 134113 (2013); M. Gerster, P. Silvi, M. Rizzi, R. Fazio, T. Calarco, and S. Montanero, *Phys. Rev. B* **90**, 125154 (2014).
- [19] S. R. White, *Phys. Rev. Lett.* **69**, 2863 (1992).
- [20] U. Schollwöck, *Ann. Phys.* **326**, 96 (2011), 1008.3477.
- [21] F. Verstraete, M. M. Wolf, D. Perez-Garcia, and J. I. Cirac, *Phys. Rev. Lett.* **96**, 220601 (2006); G. Vidal, *Phys. Rev. Lett.* **99**, 042113 (2007).
- [22] Notice that the continuum limit is also recovered by adding tailored long-range hoppings, which effectively flatten the lowest band [40].
- [23] R. B. Laughlin, *Phys. Rev. Lett.* **50**, 1395 (1983).
- [24] Q. Niu, D. J. Thouless, and Y.-S. Wu, *Phys. Rev. B* **31**, 3372 (1985); R. Tao and F. Haldane, *Phys. Rev. B* **33**, 3844 (1986).
- [25] J. Budich, A. Elben, M. Łącki, A. Sterdyniak, M. Baranov, and P. Zoller, *Phys. Rev. A* **95**, 043632 (2017).
- [26] M. C. Strinati, E. Cornfeld, D. Rossini, S. Barbarino, M. Dalmonte, R. Fazio, E. Sela, and L. Mazza, ArXiv e-prints (2016), 1612.06682 [cond-mat.quant-gas].
- [27] A. Petrescu, M. Piraud, G. Roux, I. P. McCulloch, and K. L. Hur, ArXiv e-prints (2016), 1612.05134 [cond-mat.quant-gas].
- [28] Y.-C. He, F. Grusdt, A. Kaufman, M. Greiner, and A. Vishwanath, ArXiv e-prints (2017), arXiv:1703.00430 [cond-mat.str-el].
- [29] Y.-Y. Shi, L.-M. Duan, and G. Vidal, *Phys. Rev. A* **74**, 022320 (2006).
- [30] S. Singh, R. N. C. Pfeifer, and G. Vidal, *Phys. Rev. B* **83**, 115125 (2011); A. J. Ferris, *Phys. Rev. B* **87**, 125139 (2013).
- [31] Supplementary Material.
- [32] A. Kitaev and J. Preskill, *Phys. Rev. Lett.* **96**, 110404 (2006); M. Levin and X.-G. Wen, *Phys. Rev. Lett.* **96**, 110405 (2006).
- [33] X.-G. Wen and Q. Niu, *Phys. Rev. B* **41**, 9377 (1990).
- [34] Y. Hatsugai, *J. Phys. Soc. Jpn.* **73**, 2604 (2004); *J. Phys. Soc. Jpn.* **74**, 1374 (2005).
- [35] M. Hafezi, A. S. Sørensen, M. D. Lukin, and E. Demler, *Europhys. Lett.* **81**, 10005 (2007).
- [36] S. Depenbrock, I. P. McCulloch, and U. Schollwöck, *Phys. Rev. Lett.* **109**, 067201 (2012).
- [37] H.-C. Jiang, Z. Wang, and L. Balents, *Nat. Phys.* **8**, 902 (2012).
- [38] J. Sebby-Strabley, M. Anderlini, P. S. Jessen, and J. V. Porto, *Phys. Rev. A* **73**, 033605 (2006); S. Fölling, S. Trotzky, P. Cheinet, M. Feld, R. Saers, A. Widera, T. Müller, and I. Bloch, *Nature* **448**, 1029 (2007).
- [39] bwUniCluster: funded by the Ministry of Science, Research and Arts and the universities of the state of Baden-Württemberg, Germany, within the framework program bwHPC.
- [40] E. Kapit and E. Mueller, *Phys. Rev. Lett.* **105**, 215303 (2010).
- [41] C. Hubig, I. P. McCulloch, U. Schollwöck, and F. A. Wolf, *Phys. Rev. B* **91**, 155115 (2015).

Supplemental Material

Algorithm for ground and low excited states with tree-tensor networks

The ground state search is performed according to a variational scheme, first developed in the context of DMRG/MPS ground state algorithms [20], and which in the meantime has been generalized to arbitrary loopless tensor networks (TN) geometries [18]. The basic motivation is the following: Although the TN representation of the many-body state already reduces dramatically the number of coefficients in the state vector (as compared to the full Hilbert space dimension), solving the minimization problem

$$E_0 = \langle \Psi_0 | H | \Psi_0 \rangle \stackrel{!}{=} \min. \quad (\text{S1})$$

for the entire TN state $|\Psi_0\rangle$ directly is in practice not feasible, because the number of coefficients in $|\Psi_0\rangle$ is typically still far too large to be handled by numerical eigensolvers. Instead, one applies an iterative strategy: out of all the tensors, which together constitute the TN state, only the coefficients of one (or two, dependent on the update scheme [41]) tensor(s) are considered variational, while the others are taken to be fixed. This allows one to contract the physical Hamiltonian H to a reduced, effective Hamiltonian H_{eff} , only acting on the degrees of freedom of the variational tensor(s). For loopfree TNs the resulting reduced optimization problem can again be formulated as a standard eigenvalue problem, whose size is now manageable by an eigensolver. One then successively targets all the tensors in the TN, thereby gradually decreasing the energy expectation value $\langle \Psi_0 | H | \Psi_0 \rangle$. This procedure is called *sweeping*. A sweep is completed after all the tensors in the TN have been updated once. For the tree-tensor network (TTN) architecture employed here (sketched in Fig. 1c of the main text), the ansatz contains $N_s - 2$ tensors ($N_s = L^2$: number of lattice sites) and all involved contractions (both computation of H_{eff} and solving the reduced eigenvalue problem) have computational complexity $\mathcal{O}(m^4)$ or less. Therefore, the GS algorithm runtime scales as $\mathcal{O}(N_s m^4)$. Convergence of the GS energy is typically reached after less than ten sweeps.

To determine excited states, we employ a very similar algorithm to the one just described, with the small modification that orthogonality to all previously determined eigenstates is enforced. This can be achieved by penalizing overlap with these eigenstates; more in detail, in order to obtain the n -th excited state of H (orthogonal to all lower-lying eigenstates $|\Psi_k\rangle$, $k \in [0, n - 1]$) we solve the optimization problem

$$E_n = \langle \Psi_n | H | \Psi_n \rangle + \sum_{k=0}^{n-1} \epsilon_k \langle \Psi_n | P_k | \Psi_n \rangle \stackrel{!}{=} \min. , \quad (\text{S2})$$

where $P_k = |\Psi_k\rangle\langle\Psi_k|$ is the projector on the k -th eigenstate and ϵ_k is as an energy penalty which has to be chosen large enough, which means larger than the energy difference $|E_k - E_n|$ to the target state. Of course this energy difference is not known at the start of the algorithm, but in practice one can simply estimate a value which is guaranteed to be large enough, e.g. one can set ϵ_k to be one order of magnitude larger than a typical energy scale in the system. The scaling of the computational complexity of the algorithm is not changed by the additional projective terms in Eq. (S2): In complete analogy to the effective Hamiltonian these terms lead to effective projectors, which only contribute a (typically small) overhead to the algorithm. In particular, the runtime scaling for determining excited states remains at $\mathcal{O}(N_s m^4)$.

Bond dimension convergence of observables

We exemplify the convergence of the energy expectation value as a function of the bond dimension m in Fig. S1. Estimates for finite bond dimension errors can be obtained by extrapolating to the limit $m \rightarrow \infty$. For the system sizes considered here, we reached bond dimensions of up to $m \approx 500$, typically displaying truncation errors of order of 10^{-6} .

In Fig. S2 we demonstrate bond dimension convergence for the Green functions shown in Fig. 3a of the main text.

Edge current behavior

In Fig. S3 we provide an illustration of the edge current present in an OBC lattice, which gives an intuitive (albeit over-simplified) explanation for the behavior of the current shown in Fig. 3b of the main text.

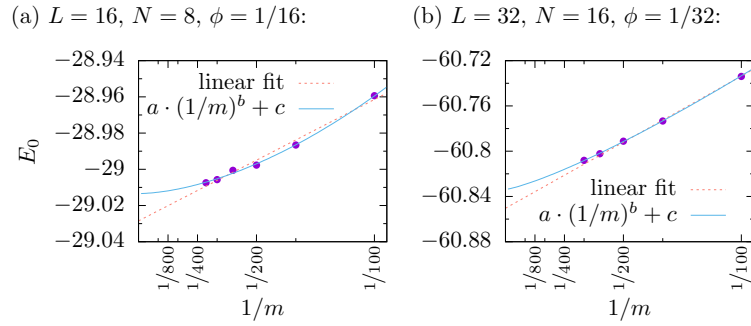


Figure S1. GS energy E_0 as a function of bond dimension m for two different system sizes $L = 16$ (a) and $L = 32$ (b). Also shown are two different $m \rightarrow \infty$ extrapolations, a simple one linear in $1/m$ and a more versatile one where the exponent of $1/m$ is allowed to be adjusted by the fit. This procedure can be used to estimate the ground state energies and corresponding errors to be $E_0 = -29.015 \pm 0.016$ (a), and $E_0 = -60.84 \pm 0.03$ (b).

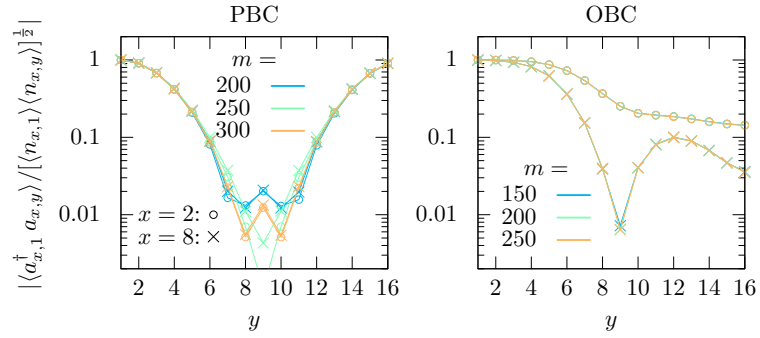


Figure S2. Bond dimension convergence of the Green functions from Fig. 3a of the main text. Different colors denote different bond dimensions, while the two different symbols refer to two different choices of x (circles: $x = 2$, crosses: $x = 8$). For PBC the different choices of x result in the same curves, as expected for a system with translational invariance; only at $y \approx L/2$ translational invariance is slightly broken, indicating a finite bond dimension error of the order of 10^{-2} .

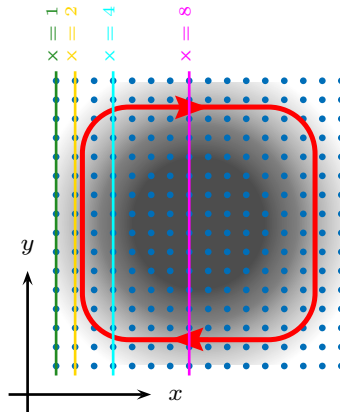


Figure S3. Illustration of the edge current in a system with OBC. The colored lines are lines of constant x , along which the x -component of the current, \mathcal{I}_x , is plotted in Fig. 3b of the main text. From this cartoon it becomes immediately clear that \mathcal{I}_x vanishes in the bulk (dark-shaded background), while at the edges (bright background) \mathcal{I}_x is nonzero whenever $y \approx 1$ or $y \approx L$. Moreover it is obvious that the sign of \mathcal{I}_x at $y \approx 1$ is opposite to the sign of \mathcal{I}_x at $y \approx L$.

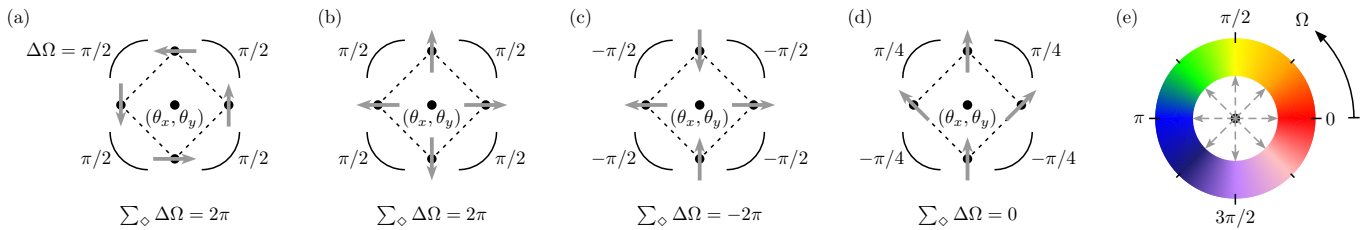


Figure S4. (a-d) Four example configurations for the argument field $\Omega_{\Phi \rightarrow \Phi'}$ around a point (θ_x, θ_y) on the boundary condition grid. The branch vortex count $1/2\pi \sum_{\diamond} \Delta\Omega$ is 1 for the configurations shown in (a) and (b), -1 for the configuration in (c), while for the one in (d) it is 0. (e) Illustration of the color code for $\Omega_{\Phi \rightarrow \Phi'}$ (used in Fig. 2d of the main text).

Procedure for determining the location of branch vortices

As described in the main text, we obtain the branch vortex count of a point (θ_x, θ_y) on the boundary condition grid by summing up the angle differences $\Delta\Omega$ of the argument field $\Omega_{\Phi \rightarrow \Phi'}$ along the four nearest neighbors of (θ_x, θ_y) . This procedure, following Refs. [34], is exemplified in Fig. S4 for four different illustrative configurations of $\Omega_{\Phi \rightarrow \Phi'}$, displaying different branch vorticities. Moreover, in Fig. S4e we provide an illustration for the color code used in Fig. 2d.

MBCN determination in the presence of the superlattice

As discussed in the main text, the GS of \tilde{H} for sufficiently deep superlattice potentials is a normal insulator, with the particles localized at the sites of the superlattice (see also Fig. S5a). This state is topologically trivial and non-degenerate. The topologically trivial character of such a GS can be evidenced by considering the quantity

$$\Gamma_{\Phi}(\theta_x, \theta_y) = \langle \Phi | \Psi_0(\theta_x, \theta_y) \rangle \langle \Psi_0(\theta_x, \theta_y) | \Phi \rangle, \quad (\text{S3})$$

where Φ represents a gauge reference, formed by a single GS at an (arbitrary) reference point $(\theta_x^{[r]}, \theta_y^{[r]})$. If the GS of the system is in fact topologically trivial, Γ_{Φ} is well-defined (i.e. non-vanishing) on the whole boundary condition torus. On the contrary, this is no longer the case if the GS has non-trivial topological character: in that case there is a finite region on the torus where Γ_{Φ} vanishes. Whenever this happens, the GS is quasi-degenerate and Hatsugai's method for determining the MBCN (as described in the main text) is applicable. In Fig. S5b we show Γ_{Φ} for different values of μ , demonstrating how it gradually becomes well-defined on the whole boundary condition torus as the depth of the superlattice potential is increased. Fig. S5c shows that the GS at $\mu = -1.0$ (just before the transition) is still quasi-degenerate, leading to a MBCN of 1; on the contrary, for $\mu = -2.0$ the GS degeneracy has been destroyed completely (see Fig. S5d), hence the MBCN is 0.

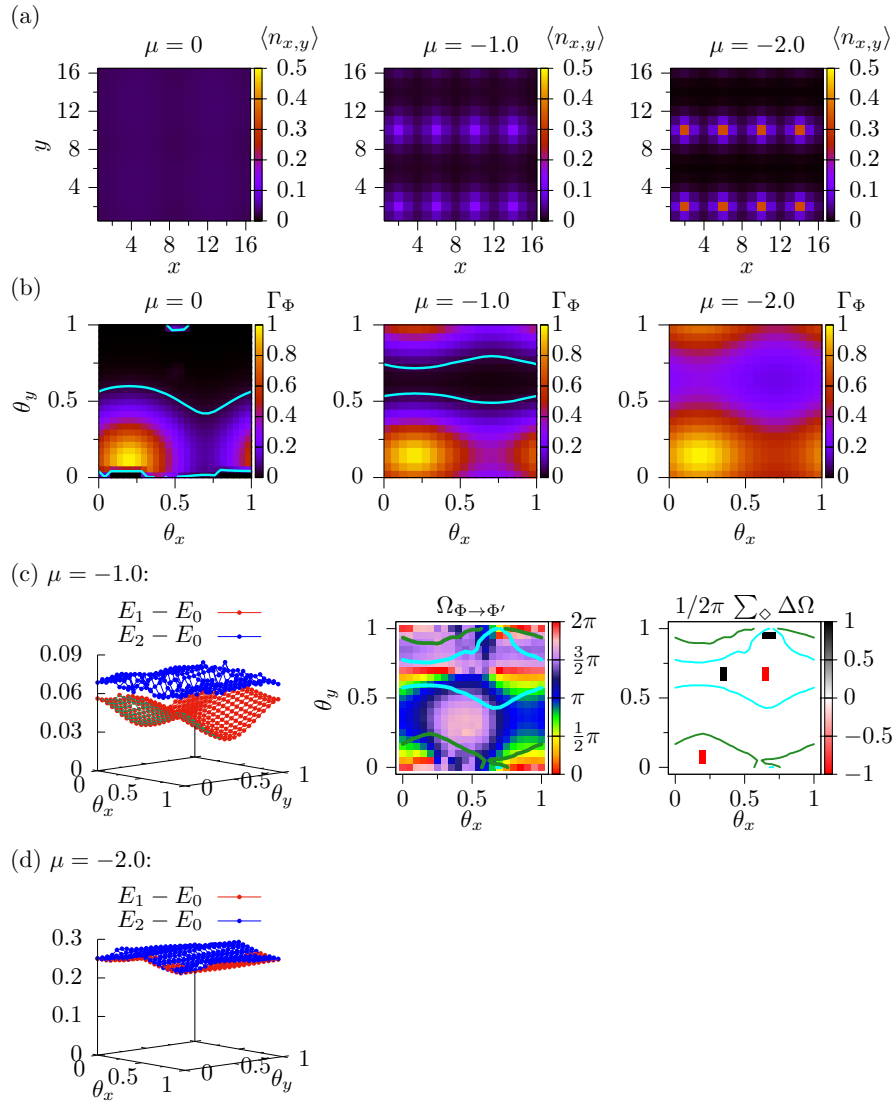


Figure S5. (a) On-site occupations $\langle n_{x,y} \rangle$ of the lattice sites for different values of μ , showing how the particles gradually localize at the energetically favored sites of the superlattice. (b) Plot of Γ_Φ for different values of μ . For $\mu \gtrsim -1.0$ there exist regions (visible as black areas enclosed by cyan lines) where Γ_Φ vanishes, indicating topologically non-trivial character. (c) Low-energy spectrum and MBCN determination for $\mu = -1.0$, resulting in MBCN = 1. (d) Low-energy spectrum at $\mu = -2.0$.